THE ASTROPHYSICAL JOURNAL, 459:259–270, 1996 March 1

OBSERVATIONS OF 4U 1700−37 WITH BATSE

B. C. RUBIN,[1] M. H. FINGER,[1,2] B. A. HARMON, W. S. PACIESAS,[3] G. J. FISHMAN, R. B. WILSON, C. A. WILSON, M. N. BROCK, M. S. BRIGGS,[3] AND G. N. PENDLETON[3]
NASA/Marshall Space Flight Center, Huntsville, AL 35812

AND

L. R. COMINSKY AND M. S. ROBERTS[4]
Department of Physics and Astronomy, Sonoma State University, Rohnert Park, CA 94928
Received 1995 June 7; accepted 1995 September 5

ABSTRACT

The eclipsing binary X-ray source 4U 1700−37 has been continually monitored by the BATSE experiment on the *Compton Gamma Ray Observatory* since the spring of 1991. Using source measurements at times of Earth occultation, we observe an average (uneclipsed) flux of 0.23 crab in the 20–120 keV band. The flux is highly variable, with occasional flaring behavior on timescales from hundreds of seconds to several hours and intensities as bright as 1 crab. The uneclipsed spectrum is well represented by an optically thin thermal bremsstrahlung model with a temperature of 25 keV independent of source intensity or orbital phase. An upper limit of 4% on the pulse fraction has been obtained for pulse periods between 2 and 700 s. Average orbital light curves from almost 1000 days of occultation measurements have been constructed. These profiles are used to measure (1) the eclipse semiangle, $\theta_E = 28.^{\circ}6 \pm 2.^{\circ}1$ in the 20–120 keV band, and (2) the decrease in orbital period, $\dot{P}/P = -(3.3 \pm 0.6) \times 10^{-6}$ yr^{-1}. Estimates of system physical parameters are obtained using Monte Carlo simulations to propagate errors in measured and assumed parameters. For the X-ray source mass we find $M_x = 2.6^{+2.3}_{-1.4}\ M_\odot$, and for the mass and radius of the optical companion, $M_O = 30^{+11}_{-7}\ M_\odot$ and $R_O = 18^{+2}_{-2}\ R_\odot$.

Subject headings: binaries: eclipsing — stars: individual (4U 1700−37) — stars: neutron — X-rays: stars

1. INTRODUCTION

The high-mass X-ray binary (HMXB) 4U 1700−37 was first detected with the *Uhuru* satellite (Jones et al. 1973). *Uhuru* observations revealed that it is an eclipsing binary with a period of 3.412 days. Optical observations of the companion HD 153919 indicate that it is an O6f star, located at a distance of about 1.8 kpc. From these observations it was inferred that HD 153919 slightly underfills its Roche lobe (Conti 1978). This implies that the X-ray source is powered by the wind of the companion star. The mass of the X-ray source is consistent with that of a neutron star (Hutchings 1974), and the high-energy spectrum is similar to that of X-ray pulsars (Dolan et al. 1980). This suggests that 4U 1700−37 is a neutron star, despite the fact that no X-ray pulsations or X-ray bursts have ever been confirmed.

The lack of a confirmed pulse period complicates the determination of system parameters. This determination is further limited by the uncertainty on the companion radial velocity semiamplitude K_O and the duration of X-ray eclipse. Here we will reexamine the system parameters based on an improved eclipse semiangle measurement.

The decrease in the orbital period, first observed by *EXOSAT* (Haberl, White, & Kallman 1989), is confirmed by our observations. Two possible causes of orbital period decrease in this system are those due to wind-driven angular momentum loss from the companion star and the tidal mechanism. By comparing our result to the expected rates of change from these sources, we find that angular momentum loss is most likely the dominant cause of the period change.

The BATSE experiment has obtained the longest continuous record of observations of 4U 1700−37, sampling its flux up to 30 times per day for over 1000 days and recording flares at 1.024 s resolution. In this paper we will examine the characteristics of the system exhibited in the long-duration BATSE database. In § 2 we present the observations. The eclipse semiangle is determined by fitting the orbital profile of the X-ray emission to a model. Using this result, the system physical parameters are calculated in § 3. The orbital period change is determined in § 4. These results are further discussed in § 5, and our conclusions are summarized in § 6.

2. OBSERVATIONS

The Burst and Transient Source Experiment (BATSE) on the *Compton Gamma Ray Observatory* (*CGRO*) is an all-sky monitor for gamma-ray bursts, persistent sources, and transient phenomena. Here we report on the analysis of data obtained with eight uncollimated NaI(Tl) large area detectors (LADs) (effective area ~ 1500 cm^2 per detector in the 20–50 keV band, sensitive to photons in the 20–1800 keV band) which are mounted in an octahedral geometry around the *CGRO* spacecraft (Fishman et al. 1989). Data with 1.024 s time resolution is telemetered to the ground in four energy channels (DISCLA data type), and with 2.048 s resolution in 16 energy channels (CONT data type).

About 85% of the sky is occulted by the Earth twice every spacecraft orbit (~ 90 minutes). When a source is sufficiently bright ($\gtrsim 300$ mcrab), the profile of Earth occultation is visible in the raw count rate data. At each Earth occultation, count rate measurements are accomplished by separately fitting each energy channel of CONT rates to a

[1] Universities Space Research Association.
[2] *CGRO* Science Support Center.
[3] Department of Physics, University of Alabama in Huntsville, Huntsville, AL 35899.
[4] Present address: Stanford University, Stanford, CA 94305.

model. The model consists of a quadratic background model plus terms for known bright sources in a 4 minute window centered on the limb crossing time of the source (Harmon et al. 1992). We call these edge fits. Each detector with its axis less than 60° to the source (between one and four detectors, but typically two) is fitted separately. The source-term profile as a function of time is determined from an energy-dependent model of the atmospheric transmission along the line of sight to the source. Typically, the transmission varies between null and full during a 20 s interval, but this interval can vary from 10 to 90 s depending on the angle of the source to the plane of the spacecraft orbit. Photon fluxes can then be obtained by convolving a spectral model through detector response matrices and fitting to the measured count rates. The 3 σ sensitivity obtained by averaging occultation edge measurements is about 100 mcrab per day.

The quadratic background model used in the edge fits is inadequate for windows longer than about 300 s. In order to represent detector background effectively on longer timescales, a global background model has been developed (Rubin et al. 1992). This model contains terms which represent backgrounds due to the diffuse cosmic background, prompt radiation caused by cosmic-ray interactions in the atmosphere and spacecraft, radioactivation of detector materials during South Atlantic Anomaly (SAA) passages, and bright occulting sources. The occulting source transmission model used in the edge fits is also used in the background model. Below we use background-subtracted DISCLA data to obtain light curves and perform timing analysis of flaring episodes. Background-subtracted data have also been used to search for coherent pulsations from 4U 1700−37.

2.1. *Light Curves of Flaring Events*

Flaring behavior from 4U 1700−37 is observed as an increase in count rate visible in the unocculted LADs facing the source. Changes on timescales from minutes to hours are observed in the DISCLA data. Isolated flaring events are observed, as well as series of flaring events lasting from hours to 2 or more days. That an increase in the background count rate is associated with a flare on 4U 1700−37 can be verified by using the relative count rates observed in different detectors to determine a sky location for a flaring event. Algorithms previously developed for locating gamma-ray bursts (Brock et al. 1992) have a statistical uncertainty of about 15° for untriggered events with significant emission between 20 and 100 keV. If several bright occultation steps are available, these can be used to verify the source location to within 0.°5.

Often a series of flares erupts over 0.5–2 days. A good example occurred while the source was uneclipsed in its binary orbit from TJD 8904.2 to TJD 8906.8. Figure 1*a* is a light curve of occultation count rates measured in DISCLA channel 1 (20–50 keV) data in LAD 3, which had a viewing angle of 19°. In this figure, occultation count rates determined from the background modeling are shown. The source is quite active during this interval, and variations by factors of 2–5 on timescales of hours are not uncommon.

These hourly variations are accompanied by rapid changes on shorter timescales. Figures 1*b*–1*d* show three episodes of fast variations, observed in the background-subtracted data of DISCLA channel 1. During this time, the background count rate varies between 800 and 1500 counts s^{-1}. In the first episode shown in Figure 1*b*, the count rate due to 4U 1700−37 remains essentially constant at a level of about 1.5 crab for 700 s, except for one spike of less than 100 s duration. The location of this spike is within 5.°0 ± 6.°2 (0.8 σ) of 4U 1700−37. In contrast, the second episode, shown in Figure 1*c*, contains large, incoherent fluctuations on timescales above 50 s. In the third episode, in Figure 1*d*, the count rate has only relatively small variations for 2500 s before increasing sharply and pulsing at least 3 times. A fourth pulse is in progress as the source is occulted by the Earth. The pulse peaks are separated by 75 s and have been located to within 25.°5 ± 16.°6 (1.5 σ) of 4U 1700−37.

As discussed in § 2.5, no clear evidence of a pulsar period for 4U 1700−37 has been found. However, in addition to the previous episode, another pulsing episode, this one containing six intense pulses, has been observed. The flare containing these pulses occurs at the peak of a series of flares lasting about 0.5 days. Background-subtracted DISCLA count rates from LAD 2 recorded during this episode are shown in Figure 2. The first pulse begins at about 81,950 s, and the pulses continue for about 550 s. The time between successive pulse peaks is about 100 s for the first five pulses and somewhat longer, about 150 s, before the last pulse. No pulses are visible in the 300 s before the source sets, although the flare is still clearly in progress. The location of the third pulse, which is the brightest, is within 20.°3 ± 10.°9 (1.9 σ) of 4U 1700−37. The setting occultation step occurs where a setting step from 4U 1700−37 is expected.

Few nearby sources which could potentially be confused with 4U 1700−37 exhibit the flaring behavior described above. Scorpius X-1 flares are visible at lower energies (in the BATSE spectroscopy detectors), but rarely above 20 keV (McNamara, Harmon, & Harrison 1995). The locations determined for the flaring events are inconsistent with the location of Scorpius X-1 at the 3 σ level or higher.

2.2. *Long-Term Light Curve*

The long-term light curve from the occultation analysis is shown in Figure 3. Each data point is the average of the 20–120 keV flux during binary phases 0.094–0.906 of one binary orbit. The horizontal dashed line is at the mean flux of 0.23 crab = 0.069 photons cm^{-2} s^{-1} (hereafter γ cm^{-2} s^{-1}), corresponding to a luminosity of 1.5×10^{36} ergs s^{-1}. The uncertainty of the mean is 0.02 crab. There are no clear long-term trends; however, the strong variability of the source is apparent. The rms scatter of the flux measurements is 0.24 crab. For comparison, BATSE occultation measurements of the Crab flux vary typically by 5%, due mainly to systematic effects.

2.3. *Spectra*

The spectrum of 4U 1700−37 has been previously measured at low energies, in the 0.5–4 keV range with *Einstein*, the 2–60 keV range with *HEAO 1* A-2 (White, Kallman, & Swank 1983), and the 2–40 keV range with *EXOSAT* (Haberl et al. 1989). Higher energy measurements, above 20 keV, can be fitted with an optically thin thermal bremsstrahlung (OTTB) model. This spectrum was observed on a balloon flight with $kT \simeq 28$ keV (Pietsch et al. 1980), with *OSO 8* with $kT \simeq 27$ keV (Dolan et al. 1980), and with SIGMA with $kT \simeq 45$ keV (Sitdikov et al. 1993). In each of these observations the shape of the source spectrum remained constant, independent of intensity or binary orbit phase. Recent observations with the *Mir Kvant* observatory

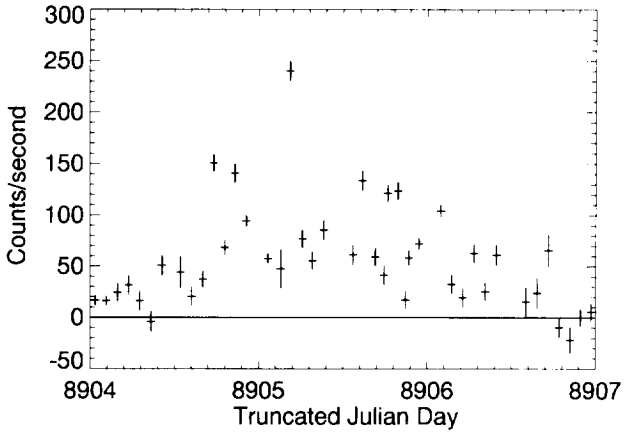

FIG. 1a

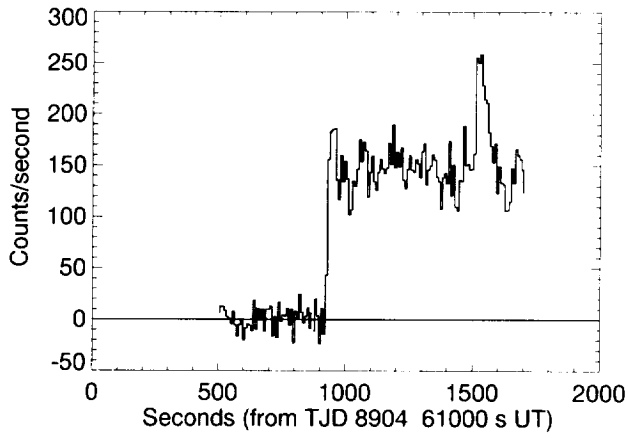

FIG. 1b

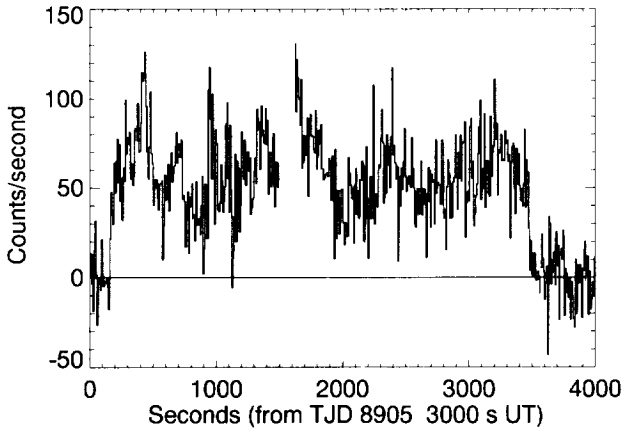

FIG. 1c

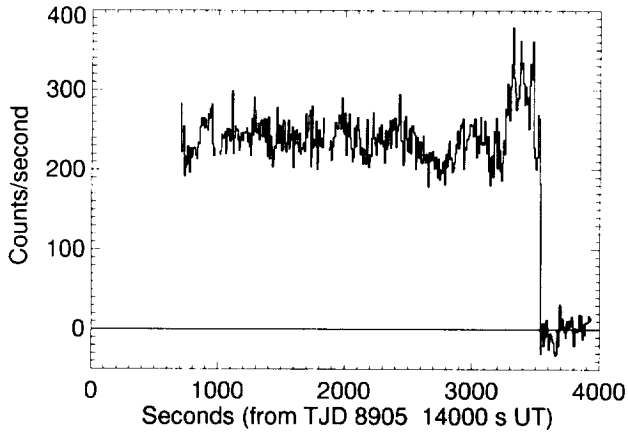

FIG. 1d

FIG. 1.—Flaring series observed during TJD 8904–8906. Data from the 20–50 keV band in LAD 3 are displayed. (*a*) Occultation count rates measured with the background model. (*b–d*) Background-subtracted count rates of flaring episodes, plotted at 8.2 s resolution. Data shown are count rates which may be attributed to 4U 1700−37. The statistical error on each data point is in the range 10–15 s. Gaps in the data are due to gaps in the telemetry. (*b*) Source rises at 927 s on the horizontal axis. (*c*) Source rises at 160 s and sets at 3480 s on the horizontal axis. (*d*) Source sets at 3530 s on the horizontal axis. Note the three pulses separated by ~75 s just before set.

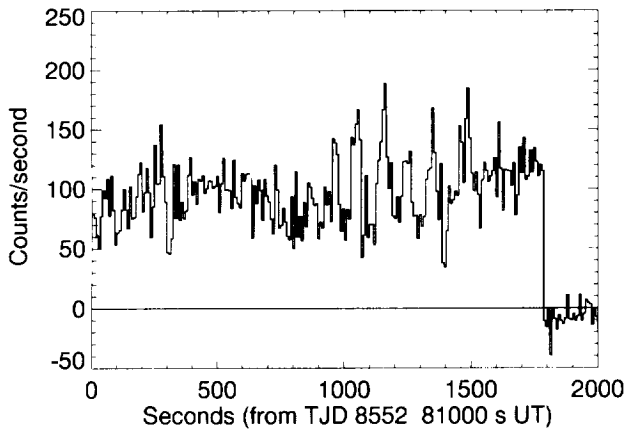

FIG. 2.—Flaring event on TJD 8552. Residual count rates from the 20–50 keV band in LAD 2 are shown. The first pulse begins at about 81,950 s, and the pulses continue for 550 s. The sharp decline at 82,785 s is a setting edge of 4U 1700−37.

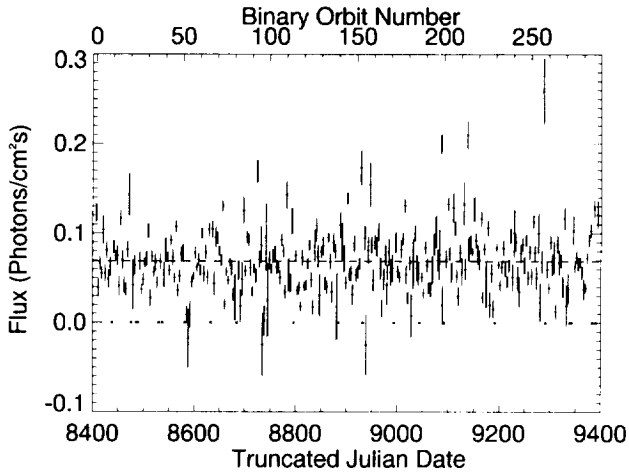

FIG. 3.—Long-term light curve. Each data point represents the average 20–120 keV uneclipsed flux in one binary orbit from the occultation analysis. Flux is averaged over binary phases 0.094–0.906. The dashed horizontal line is at the mean flux of 0.069γ cm^{-2} s^{-1}. Points without error bars at zero flux represent binary orbits in which no useful measurements were made.

in the 4–100 keV band have suggested thermal Comptonization of blackbody photons by a hot plasma as the emission mechanism (Maisack et al. 1994). The parameters of the plasma are $kT \simeq 30$ keV and optical depth $\tau \simeq 2$.

BATSE observations are consistent with these earlier results. We observe an OTTB model spectrum with a temperature of about 25 keV during all uneclipsed phases and source intensities. Figure 4 shows the uneclipsed spectrum and model averaged over a 2 week spacecraft pointing period. In this and other spectra, count rates from six channels spanning 20–120 keV were input to the fitting procedure. To make this spectrum, 166 detector steps between TJD 8450.0 and 8463.0, falling in binary phases 0.109–0.875, were used. Two detectors were fitted simultaneously. The resulting amplitude is $A = 0.223 \pm 0.014\gamma$ (cm^2 s keV)$^{-1}$ and the temperature $kT = 25 \pm 4$ keV. The reduced χ^2 is $\chi^2/\nu = 9.6/10$. For other subsets of data, the measured temperature is generally consistent with $kT = 25$ keV. The corresponding fits χ^2_ν are also close to unity.

2.4. *Orbital Profile*

Folding flux and spectral measurements from many orbits into bins of orbital phase permits construction of an average orbital profile. Both *Granat/watch* (Sazonov et al. 1993) in the 8–60 keV range and *Prognoz 9* (Kudryavstev & Svertilov 1991) in the 10–100 keV range have averaged continuous observations over many binary orbits (about 73 days and 13 months, respectively), but with low spectral resolution. Figure 5 shows the 20–120 keV BATSE flux folded into 128 phase bins. Both eclipse egress at about phase 0.1 and eclipse ingress at about phase 0.9 are clearly visible. Variations of flux with phase are due partly to flaring behavior of the source.

The average phase, ϕ_p, at which 99% of the source flux is occulted at eclipse ingress or egress, and the transition phase width τ_p, were estimated by fitting the 20–120 keV flux profile to the empirical function (Clark, Minato, & Mi 1988):

$$F_j = F_u \exp\{\ln(0.01) \exp[-(\phi_j - \phi_p)/\tau_p]\}, \quad (1)$$

where $p = i, e$ for eclipse ingress or egress, and j is the phase bin number. F_u, the average uneclipsed flux, was determined prior to the fit. The first half of the data was included for ingress, and the second half for egress.

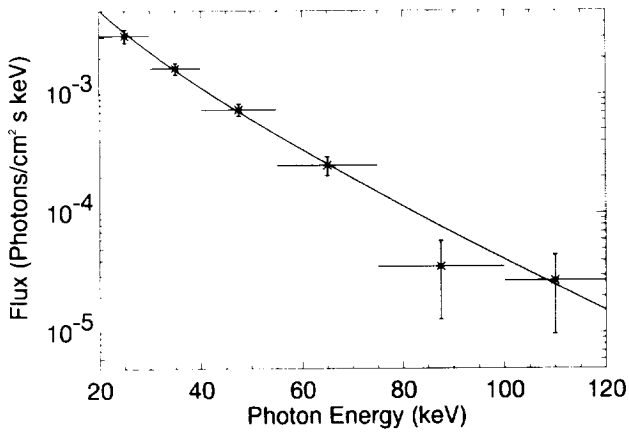

FIG. 4.—Spectrum of 4U 1700−37. Data points represent average flux observed during TJD 8450–8463 in binary phases 0.109–0.875. The solid line is the OTTB model spectrum fitted to the data. The model temperature is 25 ± 4 keV.

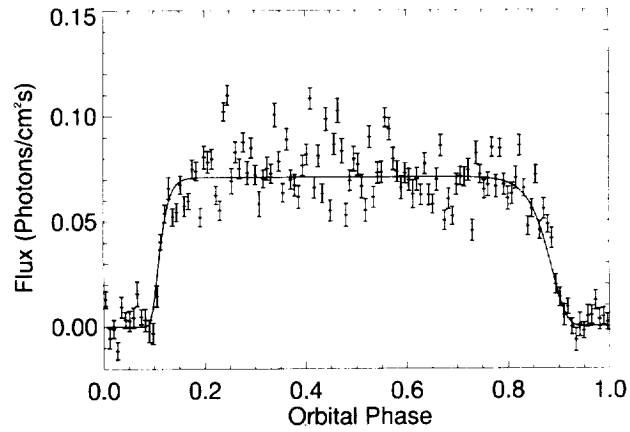

FIG. 5.—Binary orbit profile of 4U 1700−37 in the 20–120 keV range. The data were folded into 128 phase bins at the binary orbital period. The error bars during eclipse have been uniformly adjusted to reduce systematic errors in the occultation analysis. Error bars outside of eclipse have been further (uniformly) adjusted for consistency with the average uneclipsed flux. Data before and after phase 0.5 were fitted separately according to the model equation in the text. The solid curve shows the best-fit model.

To account for systematic errors in the occultation analysis and flaring behavior of the source, the error bars were uniformly adjusted before fitting, in the following manner. First, data points during X-ray eclipse were fitted to a constant flux value of zero. The error on each of the data points was multiplied by the square root of the reduced χ^2 of this fit. This factor adjusts for systematic error in the occultation measurements. Second, the uneclipsed data points, after their errors were multiplied by that factor, were fitted to a constant. The error on each uneclipsed data point was multiplied by the square root of the χ^2 of this fit to adjust for the flaring. Both systematic and flaring correction factors were typically between 1.0 and 1.5.

The model resulting from the fitting procedure is shown in Figure 5. The sizes of the error bars include the adjustments discussed above. The values of the fitted parameters in equation (1) are listed in Table 1. In constructing the orbital profile of Figure 5, we have used the ephemeris derived from BATSE data in § 4, including the orbital period derivative. The sensitivity of the profile parameters to the ephemeris has been checked by repeating the fitting procedure for periods ranging from 3.411401 to 3.411761 days in steps of 0.00003 days. This did not lead to significantly smaller transition widths than the values listed in Table 1.

The duration of X-ray eclipse can be calculated from the measured phases of ingress and egress. This duration is 0.159 ± 0.012 in phase, which is equivalent to 0.542 ± 0.040

TABLE 1

ORBITAL PROFILE FIT PARAMETERS IN THE 20–120 keV BAND[a]

Parameter	Value
ϕ_e	0.0883 ± 0.0075
τ_e	0.0122 ± 0.0038
ϕ_i	0.9295 ± 0.0091
τ_i	0.0271 ± 0.0051
χ^2_e/ν	62/64
χ^2_i/ν	46/64

[a] The parameters are in units of the orbital phase.

days. This implies an eclipse semiangle of 28°.6 ± 2°.1 in the 20–120 keV band. Evidence for a trend in eclipse duration versus energy has been searched for by dividing the 20–120 keV range into six bands and separately applying the above procedure in each band. There is no statistically significant trend with energy. The OTTB model temperature also shows no dependence on orbital phase, either near eclipse or at any time during the orbit.

The BATSE measurement represents more than a factor of 2 reduction in the uncertainty over the two previous high-energy measurements: 21° ± 10° by *OSO 8* (Dolan et al. 1980) and 26° ± 5° by *Prognoz 9* (Kudryavstev & Svertilov 1991). It is consistent with the measurement of 25° ± 6° (van Paradijs, Hammerschlag-Hensberge, & Zuiderwijk 1978) made by comparing the mideclipse time obtained from an optical light curve with the X-ray eclipse egress time determined by *Copernicus* (Branduardi, Mason, & Sanford 1978).

The width of the ingress and egress transitions are related to the distance over which source flux is occulted by dense matter. However, it should be noted that equation (1) was originally applied to individual binary eclipse transitions for which a single scale height applies. Folding data over many transitions involves the superposition of differing scale heights, and, in general, the measured widths therefore have no simple physical interpretation. With this proviso, we note from Figure 5 that eclipse ingress appears to be broader than egress. This difference which was observed by *EXOSAT* (Haberl et al. 1989), is significant in the 20–120 keV range at the 2.3 σ level. The difference is greater in the 20–30 keV band, but is not significant at higher energies. This difference may be caused by an asymmetry in the companion wind.

2.5. *Pulse Period Search*

Three previous experiments have claimed observations of X-ray pulse periods: *Copernicus* (Branduardi et al. 1978) at 24 minutes, *SAS 3* (Matilsky, La Sala, & Jessen 1978) at 97 minutes, and *Tenma* (Murakami et al. 1984) at 67.4 s. Subsequent observations by *Copernicus* (Branduardi et al. 1979) did not confirm their original observation. It was shown that the *SAS 3* observation probably arose from the effect of the 100 minute satellite period and telemetry dropouts (Hammerschlag-Hensberge, Henrichs, & Shaham 1979). The 67.4 s period was observed with *Tenma* during one flare, and is similar to the examples from BATSE data shown in § 2.1. These periods have not been observed at any other time. It is therefore unlikely that they represent a direct measurement of the pulse period. The pulsed amplitude limit from one *HEAO 1* A-2 observation (White et al. 1983) is 2% for periods between 160 ms and 480 s. Recently, SIGMA (Laurent et al. 1992) used 1 day of data to set a limit on the pulse fraction of about 0.3% on pulse periods in the neighborhood of each of the three previous claims.

Two different techniques to search for coherent pulsations in the BATSE data have been attempted. The first method uses the photon flux measurements derived from individual occultation edges. The edge measurement times were corrected to the solar system barycenter. A Lomb periodogram was performed on 4092 step measurements from uneclipsed portions of the light curve. This is necessary because these fluxes are sampled unevenly in time. No evidence for pulsations due to the source were found. This implies an upper limit on the pulse fraction of about 20% for periods between 300 s and 100 days.

Second, the DISCLA data are routinely searched for coherent pulsations by fast Fourier transform (FFT) techniques as part of BATSE daily monitoring. The absence of a clear signal detection in the direction of 4U 1700−37 implies an upper limit on the pulsed flux of about 4% of the average source flux determined from the occultation measurements for periods between 2 and 300 s. This technique becomes less sensitive for periods greater than 300 s. However, subtraction of an orbital background model from the data improves the sensitivity for pulse periods between 300 and 700 s. A search of two sets of 3 days of data, each of which contains bright outbursts, was attempted. No signal was observed during these intervals or during 1 month of routine monitoring. The upper limit on the pulsed flux remains at about 4% for a period of 700 s.

2.6. *Source Variability*

In order to view the source variability qualitatively at high frequencies, we have constructed the average power spectrum of background-subtracted DISCLA channel 1 data (20–50 keV) during TJD 8904.2–8906.8. The spectrum is the average of 102 1.024 × 512 s gapless intervals during which the source was unocculted. These intervals contain the series of flares shown in Figure 1. As can be seen in Figure 6, the power begins to rise below 40 mHz and continues to increase below 10 mHz. There are no persistent quasi-periodic oscillation (QPO) peaks present. An average power spectrum obtained during intervals when 4U 1700−37 was occulted by the Earth did not show any excess, remaining consistent with zero between 5 and 500 mHz.

The power spectrum of the pulsing episode of Figure 2 is shown in Figure 7. The pulses seen in the time domain are associated with the enhanced power around 10 mHz. Tentatively, we may call this event a transient QPO with frequency ~10 mHz and width ~5 mHz. The three pulses separated by 75 s in the flare of Figure 1*d* may be an example of the same type of transient phenomenon at a somewhat different frequency.

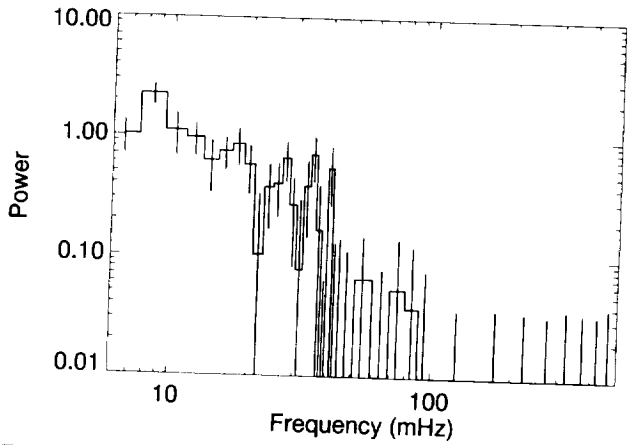

FIG. 6.—Average power spectrum of 4U 1700−37 in the 20–50 keV band observed during TJD 8904–8906 in LAD 5. The power is the square of the rms intensity per frequency interval [(rms/I)^2 Hz^{-1}], where the average intensity is the average occultation count rate observed during the interval. Positive detections are indicated by the histogram and 1 σ upper limits by error bars alone. The spectrum is the average of 102 gapless 1.024 × 512 s intervals. Frequencies above 50 mHz have been rebinned.

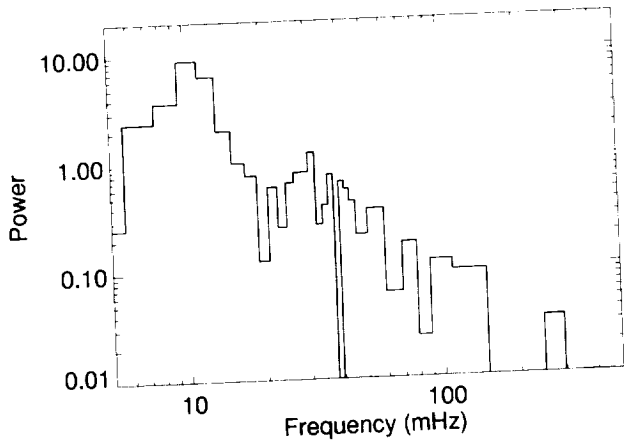

FIG. 7.—Average power spectrum during the interval between 81,629 and 82,677 s on TJD 8522. The spectrum is the average power spectrum of background-subtracted data in LADs 2 and 6 during two 512 × 1.024 s intervals. The vertical axis is in $(\mathrm{rms}/I)^2\ \mathrm{Hz}^{-1}$. The QPO feature is at a frequency of 10 mHz.

An estimate of the brightness distribution of the source can be obtained by making a histogram of the number of occultation edge measurements made as a function of flux. The measured distribution can be modeled by convolving an experimental resolution function with a model for the intrinsic flux distribution and then fitting to the measured distribution.

The flux distribution of the occultation edge measurements made at times when the X-ray source is uneclipsed (binary phase 0.125–0.875) is shown as the solid histogram in Figure 8. The peak of this distribution is at $0.065\gamma\ \mathrm{cm}^{-2}\ \mathrm{s}^{-1}$. The effect of the instrumental resolution, which must account for measured flux values below zero, is apparent.

During intervals when the source is in binary eclipse, the expected intrinsic flux probability distribution is equal to a delta function at zero flux. Using a Gaussian for the experimental resolution function and fitting to those data yields a Gaussian mean of $0.004 \pm 0.002\gamma\ \mathrm{cm}^{-2}\ \mathrm{s}^{-1}$ and a standard deviation of $0.050 \pm 0.025\gamma\ \mathrm{cm}^{-2}\ \mathrm{s}^{-1}$ with $\chi^2/\nu = 54.3/39$.

Attempting to fit the uneclipsed flux distribution to the convolution of a Gaussian resolution function with a delta function at an intrinsic flux determined by the fit leads to an intrinsic flux of $0.075 \pm 0.002\gamma\ \mathrm{cm}^{-2}\ \mathrm{s}^{-1}$ with $\chi^2/\nu = 839/88$. This is clearly an unacceptable result. Instead, an exponential model can be used for the intrinsic flux distribution:

$$P(F) = Ae^{-\alpha F}, \tag{2}$$

where F is the intrinsic flux and A is a normalization constant. This yields a standard deviation of 0.535 ± 0.0008 for the Gaussian resolution function and a value of $\alpha = 15.00 \pm 0.27$ for the exponential constant with $\chi^2/\nu = 177.5/88$. The standard deviation is consistent with that measured for the eclipsed distribution, and the χ^2 is high, but not extraordinarily so. This model is shown as the dashed curve in Figure 8.

The value of χ^2 obtained when fitting all of the uneclipsed data to an intrinsic exponential flux model could be high because that model is not a good representation of the data or because the resolution function used is not adequate. From Figure 8 we note that there is an apparent excess of flux measurements around the peak. It is thus possible that the data are consistent with an exponential model for fluxes above the peak, but that there is an excess above the exponential prediction at low flux values. To test this possibility, the exponential model fit was repeated using only the uneclipsed data with fluxes above $0.085\gamma\ \mathrm{cm}^{-2}\ \mathrm{s}^{-1}$. This results in a Gaussian standard deviation of 0.060 ± 0.004, an α of 17.50 ± 0.88, and $\chi^2/\nu = 42.3/50$. Thus, we may tentatively conclude that the distribution of flaring episodes above $\sim 0.1\gamma\ \mathrm{cm}^2\ \mathrm{s}^{-1}$ is consistent with an exponential model, but that the source also has a persistent, less intense state.

Occultation edge measurements have been used to search for evidence of correlation of spectra with intensity. First, measured edge count rates during the uneclipsed portion of the light curve were fitted to an OTTB model and the resulting fluxes ranked from brightest to dimmest. Second, average fluxes and temperatures fitted by this model were determined separately for the brightest edges in each percentile above the mean flux. The temperature measured as a function of flux in this way is shown in Figure 9. The temperature is consistent with 25 keV, the average determined for all of the uneclipsed data, independent of intensity. There appears to be a weak tendency for the temperature to be a few degrees lower for fluxes just above the mean, in comparison to more intense measurements, but this is of low significance.

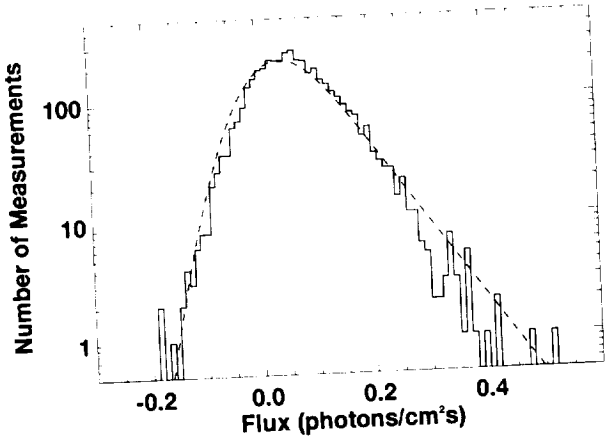

FIG. 8.—Distribution of occultation measurements as a function of flux during intervals when the X-ray source is not eclipsed by its companion. The solid histogram is the number of occultation measurements per flux bin during binary phases 0.125–0.875. The dot-dashed curve is the model resulting from the convolution of an intrinsic exponential flux distribution with a Gaussian resolution function.

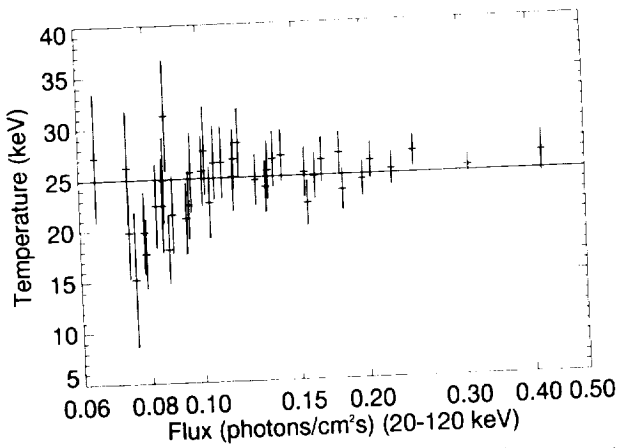

FIG. 9.—Spectral temperature vs. flux. Each data point represents an average over 1% of the occultation edge measurements. Horizontal error bars are approximately equal to the uncertainties in flux.

From the data presented in this and the previous subsections, we can establish the following conclusions about the flaring behavior: (1) flares do not occur preferentially at particular orbital phases; (2) the spectra or temperature of flares is independent of intensity; (3) significant variations occur on timescales greater than 30 s; and (4) the distribution of flare sizes above $\sim 0.1\gamma$ cm^{-2} s^{-1} is consistent with an exponential model.

3. SYSTEM PARAMETERS

The physical parameters of at least six binary systems containing X-ray pulsars, including Vela X-1 and 4U 1538−52, have been reasonably well determined from independent measurements of the orbital period, optical radial velocity semiamplitude K_O, X-ray eclipse semiangle θ_E, and projected semimajor axis of the X-ray source $a_x \sin i$. Observations of optical ellipsoidal variations were used to limit the possible range of the Roche lobe filling fraction of the companion (Rappaport & Joss 1983 and references therein). For these systems, the effects of uncertainties in the measured parameters have been propagated through formulae relating those parameters to M_x, M_O, R_O, i, and a. This has been accomplished by performing Monte Carlo simulations in which independent sets of measured parameters are randomly generated according to probability distribution for each of the derived parameters (Rappaport & Joss 1983).

This technique has not previously been applied to 4U 1700−37 because without a pulse-timing analysis, it has not been possible to measure $a_x \sin i$. Without an independent measurement of this or some other parameter, the physical parameters of this system are underdetermined.

Previous analyses (Hutchings 1974; Wolff & Morrison 1974; Heap & Corcoran 1992) have proceeded by making assumptions about the possible values or ranges of the orbital inclination i and the O star radius R_O. In particular, it is sometimes assumed that, because the source is eclipsing, i is close to 90°. However, there exists no independent evidence for the validity of this assumption, and values of i closer to 60° are just as plausible. There is some information available about the inclination of this system from measurements of the variable optical linear polarization of HD 153919 (Dolan & Tapia 1984). These measurements yield a 90% confidence interval of $71° < i < 86°$. Previous estimates or ranges for R_O have sometimes been derived from radiation-driven stellar atmosphere models and have not been independently corroborated. It is possible to set model-independent lower and upper limits to R_O from measurements of the effective temperature T_e and the optical luminosity using the relation $L_O = 4\pi R_O^2 \sigma T_e^4$, where σ is the Stefan-Boltzmann constant. Using the extreme values implied by the ranges $32{,}000 < T_e(\mathrm{K}) < 40{,}000$ and $1.2 \times 10^{39} < L_O(\mathrm{ergs\ s^{-1}}) < 4.9 \times 10^{39}$ (van Paradijs et al. 1978) leads to $12 < R_O < 40$ for R_O in solar units as a firm range for R_O.

Some previous analyses (Conti 1978) have used values of θ_E derived from lower energy experiments. However, because the flux from the source is attenuated by a wind, there should be a decreasing trend of measured eclipse duration with increasing energy. The observations, listed in Table 2, are consistent with this expectation. Moreover, lower energy measurements, and measurements averaged over only one or a few orbital cycles, are susceptible to systematic error due to the highly variable nature of the source. The source profile is not smooth, making it diffficult to fit, and the flux can fall to the eclipsed level even though the source is unocculted, leading to an overestimate of eclipse duration. Thus higher energy measurements averaged over many orbital cycles should give the most accurate estimate of θ_E.

TABLE 2

ECLIPSE SEMIANGLE AND MIDECLIPSE EPOCH MEASUREMENTS

EXPERIMENT	ENERGY RANGE θ_E keV	ENERGY RANGE θ_E Degrees	MIDECLIPSE EPOCH (JD −2,440,000)
Uhuru	2–6	58 ± 4	1453.14 ± 0.01
Copernicus	2.8–8.7	32 ± 4	2609.75 ± 0.01
Copernicus	...	...	2613.146 ± 0.01
Copernicus	...	40 ± 4	3002.104 ± 0.01
Copernicus	...	...	3005.5 ± 0.01
Copernicus and Optical	...	25 ± 6	...
OSO 8	21–84	21 ± 10	...
Prognoz 9	10–50	26 ± 5	...
EXOSAT	2–10	44.5 ± 0.6	6161.34 ± 0.0030
Granat/WATCH	8–20	37 ± 3	8723.440 ± 0.031
BATSE	20–120	28.6 ± 2.1	8651.865 ± 0.031
BATSE	...	...	9149.925 ± 0.027

Here we will reexamine the system parameters based on the improved eclipse semiangle measurement using BATSE data. Monte Carlo simulations will be used to estimate parameter probability distributions under two different sets of assumptions. The first set will be optimized for measuring the X-ray source mass. In the second set, particular values, or a range of probable values, of M_x will be assumed, and the remaining parameters estimated.

The companion Roche lobe filling fraction Ω is defined by

$$R_O = \Omega R_L , \tag{3}$$

where an approximate formula for the Roche lobe radius is (Rappaport & Joss 1983)

$$R_L/a = A - B \log q + C(\log q)^2 ; \tag{4}$$

here a is the semimajor axis of the orbit, and $q = M_O/M_x$. The coefficients A, B, C are defined by

$$A = 0.398 - 0.026\Gamma^2 + 0.004\Gamma^3 ,$$

$$B = -0.264 + 0.52\Gamma^2 - 0.015\Gamma^3 ,$$

$$C = -0.023 - 0.005\Gamma^2 ,$$

where $\Gamma = \omega_O/\omega$ is the ratio of the rotational angular frequency of the computation star to its orbital angular frequency. For a corotating system, $\Gamma = 1$. For 4U 1700−37, Γ is in the range $0.5 < \Gamma < 1.0$ (Conti & Cowley 1975; Hutchings 1974). Since HD 153919 does not overfill its Roche lobe, $\Omega < 1$. A lower limit for Ω can be set by noting that observed ellipsoidal brightness variations in optical light curves imply $\Omega > 0.8$ (van Paradijs et al. 1978).

The O star radius is related to the orbital semimajor axis, inclination, and eclipse semiangle by

$$R_O/a = \sqrt{\cos^2 i + \sin^2 i \sin^2 \theta_E} . \tag{5}$$

The companion mass function, in solar units, is determined from the measured radial velocity semiamplitude K_O (in km s^{-1}), the period P (in days), and the assumption of a circular orbit:

$$f_O = 1.038 \times 10^{-7} K_O^3 P , \tag{6}$$

where f_O is defined by

$$M_x^3 \sin^3 i = f_O(M_O + M_x)^2 . \quad (7)$$

The upper limit on the orbital eccentricity, obtained from orbital fits to UV radial velocity curves, is about 0.01 (Heap & Corcoran 1992). The semimajor axis of the binary orbit is related to the component masses by Kepler's third law:

$$a^3 = 75.19(1 + q)M_x P^2 , \quad (8)$$

where the masses and binary separation are expressed in solar units and the orbital period P is in days.

Depending on how these equations are combined, it is possible to obtain solutions for different combinations of input parameters. For example, by combining equations (3)–(5), a numerical solution for q can be determined for each set of generated values of i, Ω, Γ, θ_E, and K_O. Equation (7) then determines M_x. However, this would necessitate using an input distribution for i which contains a large uncertainty. Values of R_O determined on output by combining equations (5) and (8) could be inconsistent with the range derived from optical observations. Applying a constraint on R_O after the simulation, and retaining only parameter sets which satisfy it, would have the effect of altering the original empirical probability distributions. In general it is desirable to minimize the effect of such alterations.

Another procedure would be to generate values for R_O, Ω, Γ, θ_E, and K_O. Equation (3) then determines R_L. Combining that equation with equations (4), (5), (7), and (8) to eliminate i and M_x leads to an expression which can be solved for q numerically:

$$\Omega^2 = R_{Lr}^{-2} - 17.81P^{4/3}R_L^{-2}f_O^{2/3}(1 + q)^2 \cos^2 \theta_E , \quad (9)$$

where $R_{Lr} = R_L/a$ is a function of q and Γ by equation (4). R_O/a is found from R_{Lr} and equation (3), and then i from equation (5). Finally, M_x is determined from equation (7). Again, it is possible to obtain physically impossible solutions for which i is too small or for which $\sin i > 1.0$. The resulting inclination distribution can also be compared to the optical linear polarization measurement.

In order to optimize determination of the probability distribution for M_x, the Monte Carlo simulation generated normally distributed random values for θ_E with mean 28°.6 and standard deviation 2°.1, and for K_O with mean 18 km s^{-1} and standard deviation 3 km s^{-1}. Uniformly distributed random values were generated between 12 and 40 $R_\odot$ for R_O, between 0.5 and 1.0 for Γ, and between 0.8 and 1.0 for Ω.

Using 10,000 simulated parameter sets, we find $M_x = 2.6^{+2.3}_{-1.4}\ M_\odot$. The errors represent 1 σ confidence limits. Only 0.3% of the sets must be discarded because $\sin i > 1.0$, and 3% because $i < 55°$. However, the resulting distribution for i is peaked at 64° with only 13% of the probability between 71° and 86°, within the measured 90% confidence interval. Generating the same Monte Carlo simulation, but using a narrower range for R_O (14–25 $R_\odot$) favored by stellar atmosphere models, yields $M_x = 1.6^{+0.8}_{-0.6}\ M_\odot$. The inclination distribution is not appreciably different from the previous case. These estimates for M_x are consistent with the theoretically expected range for neutron star masses.

Because the X-ray source in this system has all the characteristics of neutron stars in systems containing a pulsar (except for pulsations), but is underdetermined by one measured parameter, we shall obtain estimates for the remaining parameters by assuming values for M_x within the theoretically expected range for neutron star masses. In order to avoid assumptions about i and R_O, they are removed from the calculation. Afterward, results for these parameters can be compared to the ranges discussed above.

The definition of f_O, equation (7), is combined with equations (3)–(5) to eliminate i and R_O and yield an expression involving Ω, M_x, q and the measured quantities θ_E and f_O:

$$\Omega^2 = R_{Lr}^{-2}[1 - (1 + q)^{4/3}(f_O/M_x)^{2/3} \cos^2 \theta_E] . \quad (10)$$

Equation (10) may be solved numerically for q (and hence M_O) for each set of generated parameters and an assumed value of M_x. The inclination is then found from equation (7), and R_O from equation (5). Finally, the expected $a_x \sin i$ (in light-seconds) is found from

$$a_x \sin i = 0.288 \frac{qK_O P}{2\pi} . \quad (11)$$

For each assumed constant value of M_x, in intervals of 0.1 $M_\odot$ between 1.2 and 3.0 $M_\odot$, 1000 simulated parameter sets were generated. Figure 10*a* shows the central value and 1 σ contours for M_O as a function of M_x, and Figure 10*b* shows the corresponding values of R_O. It is clear that the expected probable values for M_O and R_O rise as a function of M_x. Figure 10*c* shows the corresponding 1 σ contours for the inclination. The dotted lines show the 90% confidence interval from variable linear polarization. Smaller values of i are favored by the Monte Carlo simulation. The 1 σ upper limit from the simulation is below the linear polarization confidence interval for $M_x > 2.2\ M_\odot$.

The masses of five radio pulsars are known to within 0.1 $M_\odot$ and are all within the range 1.3–1.5 $M_\odot$. Uncertainties in X-ray pulsar masses are typically in the range 0.5–1 $M_\odot$. The lowest upper limit, that of Her X-1, is 1.2 $M_\odot$, and the highest lower limit, that of Vela X-1, is 1.55 $M_\odot$ (Lamb 1991). Some equations of state of neutron star matter imply a firm mass range of 1.2–1.6 $M_\odot$. Estimates for the companion parameters have been derived by performing a Monte Carlo simulation, as outlined above, with M_x drawn randomly and uniformly from the range 1.2–1.6 $M_\odot$. With 10,000 simulated events we obtain the following 1 σ results: $M_O = 30^{+11}_{-7}\ M_\odot$; $R_O = 18^{+2}_{-2}\ R_\odot$; $i = 66^{+7}_{-5}$ degrees; and $a = 31^{+3}_{-2}\ R_\odot$. The 99% confidence interval for $a_x \sin i$ is in the range 48–82 lt-s. The 99% confidence interval for R_O is in the range 13–26 $R_\odot$. There are no parameter sets for which $\sin i > 1.0$. Only 0.6% of the sets were discarded with $i < 55°$. The inclination in 0.1% of the sets are above the 90% confidence interval upper boundary of 86°, and 77% are below the lower boundary of 71°, with 11% below 60°.

Whether or not an input range is assumed for M_x the most probable values of the inclination derived from our simulations tend to be somewhat less than the lower boundary of the measured confidence interval. Repeating the last simulation, using the same input parameter distributions, except for substituting a broad uniform distribution for θ_E (23°–37°), yields almost identically the results obtained previously. This is an indication that the true inclination is probably close to or less than the low end of the measured confidence interval. More accurate measurements of the input parameters are needed to resolve this issue.

Table 3 lists the values of measured parameters and ranges of assumed parameters used in this study.

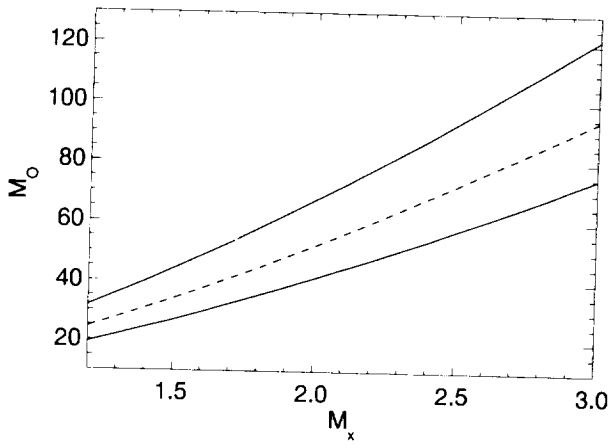

FIG. 10*a*

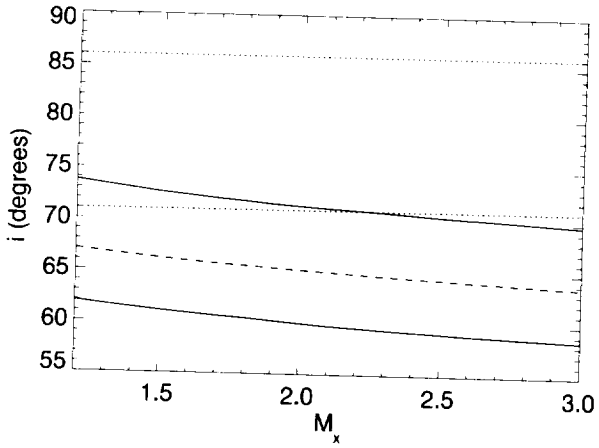

FIG. 10*c*

FIG. 10.—System parameters as a function of X-ray mass. Dashed curves show central values and solid curves represent 1 σ lower and upper limits. All quantities are in solar units. (*a*) Companion mass as a function of X-ray source mass. (*b*) Companion radius as a function of X-ray source mass. (*c*) Orbital inclination as a function of X-ray source mass. The dotted lines enclose the 90% confidence interval from variable optical linear polarization measurements.

4. ORBITAL PERIOD CHANGE

The first evidence for a change in the orbital period of 4U 1700−37 came from combining the mideclipse epoch measured by *EXOSAT* (Haberl et al. 1989) with those measured by *Uhuru* (Jones et al. 1973) and *Copernicus* (Branduardi et al. 1978). By separately applying the orbital profile fitting technique described earlier to the first and second half of the BATSE data set (about 500 days in each set), two mideclipse epochs have been derived from BATSE data. Fitting these epochs and their uncertainties together with epochs T_n days from earlier experiments to the quadratic function

$$T_n = T_0 + Pn + \tfrac{1}{2}P\dot{P}n^2 \qquad (12)$$

results in a measurement of the orbital period P in days and period derivative $\dot{P}$ at epoch T_0, where the independent variable n is an integral number of binary orbits. This yields $T_0 = \text{JD } 2{,}440{,}000 + 8900.873 \pm 0.015$; $P = 3.411581 \pm 0.000027$ days; and $\dot{P}/P = -(3.3 \pm 0.6) \times 10^{-6}$ yr^{-1} with $\chi^2 = 5.3$ for 6 degrees of freedom. A linear fit to the same data gives $\chi^2 = 159$ for 7 degrees of freedom—an unacceptable fit.

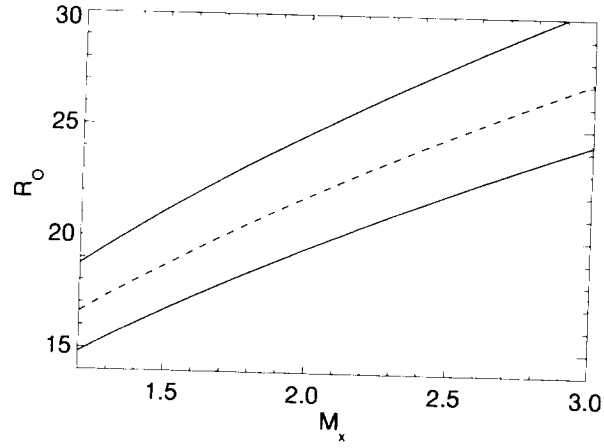

FIG. 10*b*

The measured epochs, together with the quadratic portion of the curve implied by this result, are plotted in Figure 11. Here we point out that the *Copernicus* mideclipse epoch uncertainties were not explicitly quoted by the *Copernicus* experiment, and the present calculation uses uncertainties which give a reduced χ^2 of approximately unity in a linear fit to their data. The epochs and uncertainties used are listed in Table 2.

These results are consistent both with the *EXOSAT* result ($\dot{P}/P = -(4.0 \pm 1.4) \times 10^{-6}$ yr^{-1}) and with a determination by the *Granat*/WATCH experiment ($\dot{P}/P = -(4.13 \pm 0.19) \times 10^{-6}$ yr^{-1} (Sazonov et al. 1993). However, the uncertainty quoted for the BATSE result is the formal statistical error resulting from the quadratic fit. The uncertainty quoted in the WATCH paper was determined by repeating the fit while varying the epoch of mideclipse by up to 50 orbits. In our view, for good fits, the statistical error resulting from the square root of the fit covariance-matrix element represents the minimum acceptable quotable error for quadratic fits such as these. Thus, we regard the error quoted by WATCH as an underestimate for the data plotted in Figure 11. Excluding BATSE data, we find a statistical uncertainty of 1.0×10^{-6} yr^{-1} for the WATCH observation, which has a 4.1 σ significance. Inclusion of BATSE data improves the significance of the orbital period change to 5.5 σ.

TABLE 3

4U 1700−37 SYSTEM PARAMETERS USED OR DETERMINED IN THIS STUDY[a]

Parameter	Value
θ_E	$28\overset{\circ}{.}6 \pm 2\overset{\circ}{.}1$
K_O	18 ± 3 km s^{-1}
f_O	$0.0021 \pm 0.0010\ M_\odot$
e	<0.01
Γ	$0.5 < \Gamma < 1.0$
Ω	$0.8 < \Omega < 1.0$
M_x	$2.6^{+2.3}_{-1.4}\ M_\odot$
M_O	$30^{+11}_{-7}\ M_\odot$
R_O	$18^{+2}_{-2}\ R_\odot$
i	66^{+7}_{-5} degrees
a	$31^{+3}_{-2}\ R_\odot$
$a_x \sin i$[b]	$48 < a_x \sin i$ (lt-s) < 82

[a] The uncertainties are at the 1 σ level.
[b] At the 99% confidence level.

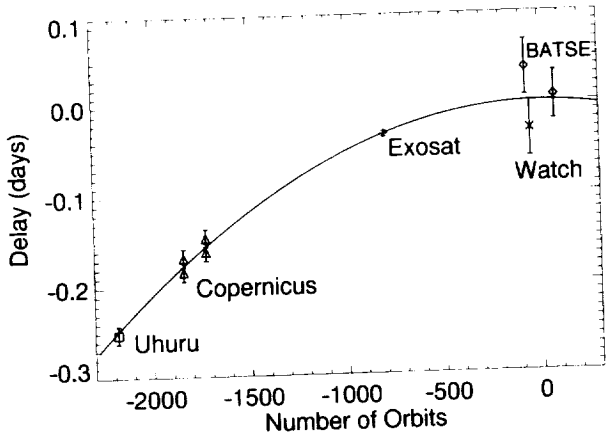

FIG. 11.—Delay in mideclipse epochs with respect to a constant orbital period. The solid line represents the quadratic portion of the best fit to the epochs.

5. DISCUSSION

The binary 4U 1700−37 is one of the most variable persistent sources which have been observed. Using BATSE, we have recorded many flaring episodes in detail and acquired a long-term history of the source. Two brief events containing clear evidence of quasi-periodic modulation with periods of 100 and 75 s appear in Figures 2 and 1*d*, respectively. These events are similar to the observation in *Tenma* data of a 67.4 s periodic signal observed in one flare (Murakami et al. 1984), and the observation of four events containing three to four pulses each, with periods between 96 and 248 s in *EXOSAT* data (Doll & Brinkman 1987). The signal observed by *Tenma* had a duration of ~1200 s and occurred at binary orbit phase 0.33, whereas the BATSE detections were at phases 0.16 with duration 550 s (100 s pulses) and 0.42 with duration at least 250 s (75 s pulses).

Here we propose that these episodes may be caused by a beat frequency model (BFM) mechanism operating in a transient accretion disk near the X-ray source. In the BFM, the Kepler motion of a series of clumps orbiting the neutron star at the magnetopause accrete onto the neutron star, producing a modulation at the beat (QPO) frequency between the Keplerian rotation frequency at the magnetosphere and the rotation frequency of the neutron star (Alpar & Shaham 1985). In this picture the magnetospheric radius contracts as the mass accretion rate (and luminosity) increase. This could explain the different frequencies observed if there is a correlation between the QPO frequency and the luminosity. Because there is no permanent disk structure in this source, these events are only observed during intervals when sufficient material accumulates just outside the magnetopause. Although BFM was first applied to low-mass X-ray binaries (LMXBs), it has recently been tentatively identified during an outburst of the Be binary source A0535+262 (Finger et al. 1995). We have searched 10 of the brightest flares in the BATSE database, and all of the data during TJD 8408–8511, but have not found evidence for additional QPO events. To test the BFM mechanism, it will be necessary to observe enough events to establish a correlation of QPO frequency with luminosity.

The expectation for wind-fed sources such as Vela X-1 and 4U 1538−52 that $P_s \propto P_{\rm orb}^{4/7}$ (Waters & van Kerkwijk 1989) would imply a spin period for 4U 1700−37 in the range of $P_s \simeq 150$–500 s. The lack of detection of pulsations implies either that the pulse period is very different from this expectation or that there is some other reason why pulses are not observed. This could be due to a chance alignment of the magnetic and rotation axes.

The long-term monitoring of 4U 1700−37 by the BATSE Earth occultation technique presented here has led to an improved measurement of the eclipse duration and ephemeris of this system. In interpreting these results, we have used the restriction $0.8 < \Omega < 1.0$ derived from ellipsoidal brightness variations observed in optical light curves. This constraint has not generally been used in previous analyses. For example, Heap & Corcoran (1992) assumed $i = 90°$ and $R_O = 17\ R_\odot$. They noted that a value for M_O of $27\ M_\odot$ is a factor of 2 lower than the masses of single stars of similar spectral type and position on the H-R diagram. The low mass implies stellar wind parameters which are different from those of single O stars, and therefore either the mass of the companion must be a factor of 2 larger or winds in high-mass X-ray binaries (HMXBs) are different from those of single O stars. Those authors suggest that this problem can be resolved if the eclipse semiangle is close to 30°. Their other assumptions lead to $M_O = 52\ M_\odot$, $q = 29$, and $a = 2R_O$. Their scenario implies a small value of Ω less than 0.77. Using Monte Carlo error propagation techniques, and assuming a neutron star mass consistent with those in other systems, we have shown that the question of whether the O star is undermassive cannot be firmly resolved. However, the data do favor smaller masses.

An orbital period change has been observed for only two other HMXBs: Cen X-3 (Nagase et al. 1992) and SMCX-1 (Levine et al. 1993). The system parameters and orbital period change determined in this paper can be used to assess the cause of the orbital period change. This change could be caused by wind-driven angular momentum loss, or by tidal interactions, or by a combination of both.

Our results can be compared to a recent ballistic (numerical) calculation of the contribution of wind-driven angular momentum loss to orbital period changes in high-mass binary systems. The relation between the rate of orbital period change, the mass-loss rate of the companion, the average angular momentum loss per unit mass of wind particles in the center of mass of the binary system ($h_{\rm cm}$), and the mass ratio q is (Brookshaw & Tavani 1993, hereafter BT):

$$\frac{\dot{P}}{P} = -3\left(1 - h_{\rm cm} - \frac{1}{3}\frac{q}{1+q}\right)\frac{\dot{M}_O}{M_O}, \qquad (13)$$

where the mass fraction of the wind captured by the primary is assumed to be negligible for this purpose.

Tables of $h_{\rm cm}$ as a function of q, Ω, and wind velocity V normalized to the orbital velocity of the secondary around the center of mass, $V_{\rm cm} = a\omega/(1+q)$, have been compiled by BT. From our results we may take $V_{\rm cm} = 20 \pm 3$ km s^{-1}. The escape velocity of the wind is 617 km s^{-1}, and the terminal velocity (Heap & Corcoran 1992) is 2100 km s^{-1}, which imply normalized velocities $V = 31 \pm 5$ and $V = 106 \pm 28$, respectively. From Table 1 of BT, at large velocities ($V > 30$) $h_{\rm cm}$ apparently approaches a nearly constant value, and changes negligibly with velocity but increases with q. From Table 13 of BT, it is apparent that $h_{\rm cm}$ also increases with Ω. For $q = 30$, $\Omega = 1$, BT find $h_{\rm cm} = 9.5$. If we also use $\dot{M}_O = -6 \times 10^{-6}\ M_\odot$ yr^{-1} (Haberl et al. 1989) and $M_O = 42\ M_\odot$, then equation (13) yields an orbital

period change $\dot{P}/P = -3.8 \times 10^{-6}$ yr^{-1}, within 1 σ of our measurement. Thus we cannot rule out the possibility that the period change is due entirely to angular momentum loss in the stellar wind. However, we note that the results presented in BT assume corotation of the companion with the binary orbit. Recently, h_{cm} has been calculated as a function of Γ (M. Tavani 1995, private communication). In general, h_{cm} increases with Γ. The smallest possible value of h_{cm} for this system, at $q = 15$, $\Omega = 0.8$, $\Gamma = 0.5$, is $h_{cm} = 1.5$. Assuming also $M_O = 20\ M_\odot$ implies an orbital period decrease due to mass loss which is 25% of that observed. Allowing also for a $\sim 50\%$ uncertainty in $\dot{M}_O$, we set a lower limit of 10% on the contribution of mass loss to the observed orbital decrease. Thus, considering also the $q = 30$, $\Omega = 1$, $\Gamma = 1$ case discussed above, we conclude that ballistic calculations imply that between one-tenth and all of the observed orbital period decrease is due to mass loss by the companion star.

As an additional complication we note that these ballistic calculations do not include the radiative forces acting on the wind. How this impacts the calculation of wind-driven orbital angular momentum loss depends on the details of the accretion. The velocity law which is usually assumed is of the form $v = v_\infty(1 - R_O/r)^\alpha$, where v_∞ is the terminal wind velocity, α is the wind acceleration parameter, and r is the distance from the center of the secondary star. This wind is, however, disturbed by the presence of the X-ray source, which photoionizes surrounding material, decreasing the radiative cross section and stopping the radiative acceleration in some region (Strömgren sphere) around the X-ray source. Haberl et al. (1989) fitted *EXOSAT* data to the observed column density as a function of phase. They found $\alpha = 0.43$ and a dimensionless ionization parameter $\xi = 190$, which measures the size of the Strömgren sphere. With these values, the wind reaches escape velocity at about $r = 1.1R_O$, while the Strömgren sphere does not begin until about $r = 1.4R_O$. Thus, if these parameters are approximately correct, neither the radiative acceleration nor the X-ray photoionization should have an appreciable impact on the mass-loss calculation.

The contribution of tidal interactions to the orbital period change can be estimated by computing the circularization time for a radiatively damped tide (Lecar, Wheeler, & McKee 1976, eq. [19]). For the central measured parameter values of 4U 1700−37, we find that $t_{circ} = 7 \times 10^6$ yr. Propagating 1 σ errors on the measured quantities shows that the tidal mechanism can supply $4.3^{+8.1}_{-2.9}$ percent of the orbital period change. That is, the 1 σ upper limit is about 12.4% and the central value is about 4.3%. The 95% confidence upper limit is 21%. This is consistent with the above result that the period change due to mass loss is between 10% and 100% of the total. Thus it appears likely that in this system mass loss is the dominant cause of the orbital period change.

6. CONCLUSION

Summing almost 1000 days of BATSE occultation data has permitted determination of the eclipse semiangle of 4U 1700−37 with a 1 σ uncertainty of about 2°. This measurement, combined with the optical and UV measurements of the radial velocity semiamplitude, a range constraint on the Roche lobe filling factor, and the assumption of a circular orbit have led to a new determination of the system parameters. Propagation of errors on experimental quantities shows that the mass of the X-ray source is very probably within the theoretically expected range for neutron stars. The question of whether the companion is undermassive cannot at this time be firmly resolved, but the evidence does favor smaller masses. No evidence for a coherent pulse period between 2 and 700 s has been observed.

An OTTB model spectrum with a temperature of 25 keV is consistent with BATSE data, independent of source intensity or orbital phase. Observations of flaring behavior show variations on timescales from 30 s to more than 1 day. The distribution of flare sizes is consistent with an exponential model. Transient events of a quasi-periodic nature observed in BATSE data as well as by other experiments hint at the possible formation of transient disk structures.

Combining two mideclipse epochs determined from BATSE data with those determined from earlier experiments leads to a value for the rate of orbital period decrease which is significant at the 5.5 σ level. The contribution of mass loss in the companion wind to this decrease is between 10% and 100%, while the contribution from tidal interactions is probably less than 20%.

BATSE occultation observations of 4U 1700−37 over the next 5 years will permit a further reduction of the uncertainty in θ_E and continued monitoring of the orbital period change. Accurate measurements of θ_E by other experiments and improved measurements of other parameters are needed to sharpen the determination of the system parameters. In addition, higher time resolution measurements of the orbital cycle could do more to reduce uncertainty in the orbital period change.

We thank Jan van Paradijs for useful discussions about the system parameters, and Marco Tavani for valuable discussions about the interpretation of the orbital period change.

REFERENCES

Alpar, M. A., & Shaham, J. 1985, Nature, 316, 239
Branduardi, G., Dupree, A. K., Sanford, P. W., & Pollard, G. S. G. 1979, Nature, 279, 508
Branduardi, G., Mason, K. O., & Sanford, P. W. 1978, MNRAS, 185, 137
Brock, M. N., Fishman, G. J., Meegan, C. A., Wilson, R. W., Pendleton, G. N., Stollberg, M. T., & Paciesas, W. S. 1992, in AIP Conf. Proc. 280, *Compton Gamma-Ray Observatory*, ed. M. Friedlander, N. Gehrels, & D. J. Macomb (New York: AIP), 709
Brookshaw, L., & Tavani, M. 1993, ApJ, 410, 719 (BT)
Clark, G. W., Minato, J. R., & Mi, G. 1988, ApJ, 324, 974
Conti, P. S. 1978, A&A, 63, 225
Conti, P. S., & Cowley, A. P. 1975, ApJ, 200, 144
Dolan, J. F., Coe, M. J., Crannel, C. J., Dennis, B. R., Frost, K. J., Maurer, G. S., & Orwig, L. E. 1980, ApJ, 238, 238
Dolan, J. F., & Tapia, S. 1984, A&A, 139, 249
Doll, H., & Brinkman, W. 1987, A&A, 173, 86
Fishman, G. J., et al. 1989, in Proc. *Gamma-Ray Observatory* Science Workshop, ed. W. N. Johnson (Greenbelt: GSFC), 2-39
Finger, M. H., Wilson, R. B., & Harmon, B. A. 1996, ApJ, in press
Haberl, F., White, N. E., & Kallman, T. R. 1989, ApJ, 343, 409
Hammerschlag-Hensberge, G., Henrichs, H. F., & Shaham, J. 1979, ApJ, 228, L75
Harmon, B. A., et al. 1992, in AIP Conf. Proc. 280, *Compton Gamma-Ray Observatory*, ed. M. Friedlander, N. Gehrels, & D. J. Macomb (New York: AIP), 314
Heap, S. R., & Corcoran, M. S. 1992, ApJ, 387, 340
Hutchings, J. B. 1974, ApJ, 192, 677
Jones, C., Forman, W., Tananbaum, H., Schreier, E., Gursky, H., Kellogg, E., & Giacconi, R. 1973, ApJ, 181, L43
Kudryavstev, M. I., & Svertilov, S. I. 1991, Soviet Astron., 17(3), 175

Lamb, F. K. 1991, in ASP Conf. Ser. 20, Frontiers of Stellar Evolution: McDonald Observatory 50th Anniversary, ed. D. Lambert (San Francisco: ASP), 299
Laurent, P., et al. 1992, A&A, 260, 237
Lecar, M. J., Wheeler, J. C., & McKee, C. F. 1976, ApJ, 205, 556
Levine, A., Rappaport, S., Deeter, J. E., Boynton, P. E., & Nagase, F. 1993, ApJ, 410, 328
Maisack, M., Kendziorra, E., Pan, H. C., Skinner, G. K., Pietsch, W., Reppin, C., Efremov, V., & Sunyaev, R. 1994, A&A, 283, 841
Matilsky, T., La Sala, J., & Jessen, J. 1978, ApJ, 224, L119
McNamara, B. J., Harmon, B. A., & Harrison, T. E. 1995, A&AS, 111, 587
Murakami, T., Kawak, N., Makashima, K., & Mitani, K. 1984, PASJ, 36, 691
Nagase, F., Corbet, R. H. D., Day, C. S. R., Inoue, H., Takeshima, T., & Yoshida, K. 1992, ApJ, 396, 147
Pietsch, W., Voges, W., Reppin, C., Trumper, J., Kendizorra, E., & Staubert, R. 1980, ApJ, 327, 964
Rappaport, S. A., & Joss, P. C. 1983, in Accretion-driven Stellar X-Ray Sources, ed. W. H. G. Lewin & E. P. J. van den Heuvel (Cambridge: Cambridge University Press), 1
Rubin, B. C., et al. 1992, in AIP Conf. Proc. 280, *Compton Gamma-Ray Observatory*, ed. M. Friedlander, N. Gehrels, & D. J. Macomb (New York: AIP), 1127
Sazonov, S. Y., Lapshov, I. Y., Sunyaev, R. A., Brandt, S., Lund, N., & Castro-Tirado, A. 1993, Soviet Astron., 19(4), 272
Sitdikov, M. R., et al. 1993, Soviet Astron., 19(3), 188
van Paradijs, J. A., Hammerschlag-Hensberge, G., & Zuiderwijk, E. J. 1978, A&AS, 31, 189
Waters, L. B., & van Kerkwijk, M. H. 1989, A&AS, 223, 196
White, N. E., Kallman, T. R., & Swank, J. H. 1983, ApJ, 269, 264
Wolff, S. C., & Morrison, N. D. 1974, ApJ, 187, 69